

NAISR: A 3D Neural Additive Model for Interpretable Shape Representation

Yining Jiao
UNC-Chapel Hill
jyn@cs.unc.edu

Carlton Zdanski
UNC-Chapel Hill
zdanski@med.unc.edu

Julia Kimbell
UNC-Chapel Hill
julia_kimbell@med.unc.edu

Andrew Prince
UNC-Chapel Hill
andrew.prince@unchealth.unc.edu

Cameron Worden
UNC-Chapel Hill
cameron.worden@unchealth.unc.edu

Samuel Kirse
Wake Forest School of Medicine
kirse.sam@gmail.com

Christopher Rutter
The Ohio State University College of Medicine
Christopher.Rutter@osumc.edu

Benjamin Shields
UNC-Chapel Hill
bhs@email.sc.edu

William Dunn
UNC-Chapel Hill
willad@live.unc.edu

Jisan Mahmud
UNC-Chapel Hill
jisan@cs.unc.edu

Marc Niethammer
UNC-Chapel Hill
mn@cs.unc.edu

Abstract

Deep implicit functions (DIFs) have emerged as a powerful paradigm for many computer vision tasks such as 3D shape reconstruction, generation, registration, completion, editing, and understanding. However, given a set of 3D shapes with associated covariates there is at present no shape representation method which allows to precisely represent the shapes while capturing the individual dependencies on each covariate. Such a method would be of high utility to researchers to discover knowledge hidden in a population of shapes. We propose a 3D Neural Additive Model for Interpretable Shape Representation (NAISR) which describes individual shapes by deforming a shape atlas in accordance to the effect of disentangled covariates. Our approach captures shape population trends and allows for patient-specific predictions through shape transfer. NAISR is the first approach to combine the benefits of deep implicit shape representations with an atlas deforming according to specified covariates. Although our driving problem is the construction of an airway atlas, NAISR is a general approach for modeling, representing, and investigating shape populations. We evaluate NAISR with respect to shape reconstruction, shape disentanglement, shape evolution, and shape transfer for the pediatric upper airway. Our experiments demonstrate that NAISR achieves competitive shape reconstruction performance while retaining interpretability. Our code is available at <https://github.com/uncbiag/NAISR>.

1. Introduction

Deep implicit functions (DIFs) have emerged as efficient representations of 3D shapes [37, 33, 29, 62], deformation fields [55], images and videos [44], graphs, and manifolds [16]. For example, DeepSDF [37] represents shapes as the level set of a signed distance field (SDF) with a neural network. In this way, 3D shapes are compactly represented as continuous and differentiable functions with infinite resolution. In addition to representations of geometry such as voxel grids [57, 59, 58], point clouds [1, 65, 66] and meshes [19, 53, 71], DIFs have emerged as a powerful paradigm for many computer vision tasks. DIFs are used for 3D shape reconstruction [37, 29, 44], generation [15], registration [13, 69, 46, 55], completion [37], editing [61] and understanding [36].

Limited attention has been paid to shape analysis with DIFs. Specifically, given a set of 3D shapes with a set of covariates attributed to each shape, a shape representation method is still desired which can precisely represent shapes and capture dependencies among a set of shapes. Such a representation could greatly help researchers understand shape population. There is currently no shape representation method that can quantitatively capture how covariates geometrically and temporally affect a population of 3D shapes;

neither on average nor for an individual. However, capturing such effects is desirable as it is often difficult and sometimes impossible to control covariates (such as age, sex, and weight) when collecting data. Further, understanding the effect of such covariates is frequently a goal of medical studies. Therefore, it is critical to be able to disentangle covariate shape effects on the individual and the population-level to better understand and describe shape populations. Our approach is grounded in the estimation of a shape atlas (i.e., a template shape) whose deformation allows to capture covariate effects and to model shape differences. Taking an airway atlas as an example, a desired atlas representation should be able to answer the following questions:

- Given an atlas shape, how can one accurately represent shapes and their dependencies?
- Given the shape of an airway, how can one disentangle covariate effects from each other?
- Given a covariate, e.g., age, how does an airway change based on this covariate?
- Given a random shape, how will the airway develop after a period of time?

To answer these questions, we propose a Neural Additive Interpretable Shape Representation (NAISR), an interpretable way of modeling shapes associated with covariates via a shape atlas. Tab. 1 compares NAISR to existing shape representations with respect to the following properties:

- **Representation** relates to how a shape is described. Generally, a shape can be represented explicitly (e.g., as point clouds, voxels, and meshes) and implicitly with a function, e.g., parameterized by a neural network. Implicit representations are desirable as they naturally adapt to the size of a shape and also allow shape completion (i.e., reconstructing a complete shape from a partial shape, which is common in medical scenarios) with no additional effort.
- **Deformable** captures if a shape representation results in point correspondences between shapes, e.g., via a displacement field. Specifically, we care about point correspondences between the target shapes and the atlas shape. A deformable shape representation helps to relate different shapes.
- **Disentangleable** indicates whether a shape representation can disentangle individual covariate effects for a shape. These covariate-specific effects can then be composed to obtain the overall displacement of an atlas/template shape.

- **Evolvable** denotes whether a shape representation can evolve shapes based on changes of a covariate, capturing the influence of *individual* covariates on shape.
- **Transferable** indicates whether shape changes can be transferred to a given shape. E.g., one might want to edit an airway based on a simulated surgery and predict how such a surgical change manifests later in life.
- **Interpretable** indicates a shape representation that is simultaneously *deformable*, *disentangleable*, *evolvable*, and *transferable*. Such an interpretable model is applicable to tasks ranging from the estimation of disease progression to assessing the effects of normal aging or weight gain on shape.

NAISR is the first shape representation method to investigate an atlas-based representation of 3D shapes in a deformable, disentangleable, transferable and evolvable way. We test NAISR on a 3D airway shape dataset. However, NAISR is a general method to represent and investigate shapes in an interpretable way.

2. Related Work

Deep Implicit Functions. Compared with geometry representations such as voxel grids [57, 59, 58], point clouds [1, 65, 66] and meshes [19, 53, 71], DIFs are able to capture highly detailed and complex 3D shapes using a relatively small amount of data [37, 31, 69, 46, 13]. They are based on classical ideas of level set representations [40, 34]; however, whereas these classical level set methods represent the level set function on a grid, DIFs parameterize it as an actual continuous function, e.g., by a neural network. Hence, DIFs are not reliant on meshes, grids, or a discrete set of points. This allows them to efficiently represent natural-looking surfaces [18, 44, 32]. Further, DIFs can be trained on a diverse range of data (e.g., shapes and images), making them more versatile than other shape representation methods. This makes them useful in applications ranging from computer graphics, to virtual reality, and robotics [15, 61, 38, 41]. We therefore formulate NAISR based on DIFs.

Point Correspondence. Establishing point correspondences is important to help experts to detect, understand, diagnose, and track diseases. Recently, ImplicitAtlas [64], DIF-Net [13], DIT [69], and NDF [46] were proposed to capture point correspondence within implicit shape representations. Dalca et al. [11] use templates conditioned on covariates for image registration. However, they did not explore covariate-specific deformations, shape representations or shape transfer. Currently no continuous shape representation which models the effects of covariates exists. NAISR will provide a model with such capabilities.

Method	Representation	Deformable	Disentangleable	Evolvable	Transferable	Interpretable
ConditionalTemplate [11]	Voxels	✓	✗	✓	✗	✗
3DAttriFlow [54]	Point Clouds	✓	✗	✓	✗	✗
DeepSDF [37]	Implicit	✗	✗	✗	✗	✗
A-SDF [31]	Implicit	✗	✗	✓	✓	✗
DIT [69], DIF [13], NDF [46]	Implicit	✓	✗	✗	✗	✗
NASAM [52]	Implicit	✓	✗	✓	✗	✗
Ours (NAISR)	Implicit	✓	✓	✓	✓	✓

Table 1. Comparison of shape representations in the literature based on the desirable properties discussed in Sec. 1. A ✓ indicates that a model has the desired property; a ✗ indicates that it does not. Only our NAISR model has all the desired properties.

Disentangled Representation Learning Disentangled representation learning (DRL) has been explored in a variety of domains, including computer vision [42, 14, 68, 67, 60, 63], natural language processing [21], and medical image analysis [6, 4]. DRL has also emerged in the context of implicit representations as a promising approach for 3D computer vision. By disentangling the underlying factors of variation, such as object shape, orientation, and texture, DRL can facilitate more effective 3D object recognition, reconstruction, and manipulation [45, 68, 67, 60, 63, 61, 15, 47].

Besides DRL in computer vision, medical data is typically associated with various covariates which should be taken into account during analyses. Taking [9] as an example, when observing a tumor’s progression, it is difficult to know whether the variation of a tumor’s progression is due to time-varying covariates or due to treatment effects. Therefore, being able to disentangle different effects is highly useful for a representation to promote understanding and to be able to quantify the effect of covariates on observations. *NAISR will provide a disentangled representation and will allow us to capture the shape effects of covariates.*

Articulated Shapes There is significant research focusing on articulated shapes, mostly on humans [35, 8, 50, 12]. There is also a line of work on articulated general objects, e.g., A-SDF [31] and NASAM [52]. A-SDF [31] uses articulation as an additional input to control generated shapes, while NASAM [52] learns the latent space of articulation without articulation as supervision.

The aforementioned works on articulated objects assume that each articulation affects a separate object part. This is easy to observe, e.g., the angles of the two legs of a pair of eyeglasses. Hence, although A-SDF [31] and 3DAttriFlow [54] can disentangle articulations from geometry, they do not disentangle different covariates and their disentanglements are not composable. However, in medical scenarios, covariates often affect shapes in a more entangled and complex way, for example, a shape might simultaneously be influenced by sex, age, and weight. *NAISR will allow us to*

account for such complex covariate interactions.

Explainable Artificial Intelligence The goal of explainable Artificial Intelligence (XAI) is to provide human-understandable explanations for decisions and actions of an AI model. Various flavors of XAI exist, including counterfactual inference [5, 30, 48, 7], attention maps [70, 22, 56], feature importance [3, 39, 2], and instance retrieval [10]. NAISR is inspired by neural additive models (NAMs) [2] which in turn are inspired by generalized additive models (GAMs) [20]. NAMs are based on a linear combination of neural networks each attending to a single input feature. NAISR extends this concept to interpretable 3D shape representations. This is significantly more involved as, unlike for NAMs and GAMs, we are no longer dealing with scalar values, but with 3D shapes. *NAISR will provide interpretable results by capturing spatial deformations with respect to an estimated atlas shape such that individual covariate effects can be distinguished.*

3. Method

This section discusses our NAISR model and how we obtain the desired model properties of Section 1.

3.1. Problem Description

Consider a set of shapes $\mathcal{S} = \{\mathcal{S}^k\}$ where each shape \mathcal{S}^k has an associated vector of covariates $\mathbf{c} = [c_1, \dots, c_i, \dots, c_N]$ (e.g., age, weight, sex). Our goal is to obtain a representation which describes the entire set \mathcal{S} while accounting for the covariates. Our approach estimates a template shape, \mathcal{T} (the shape atlas), which approximates the entire set \mathcal{S} . Specifically, \mathcal{T} is deformed based on a set of displacement fields $\{\mathcal{D}^k\}$ such that the individual shapes $\{\mathcal{S}^k\}$ are approximated well by the transformed template.

A displacement field \mathcal{D}^k describes how a shape is related to the template shape \mathcal{T} . The factors that cause this displacement may be directly observed or not. For example, observed factors may be covariates such as subject age, weight, or sex; i.e., \mathbf{c}_k for subject k . Factors that are not

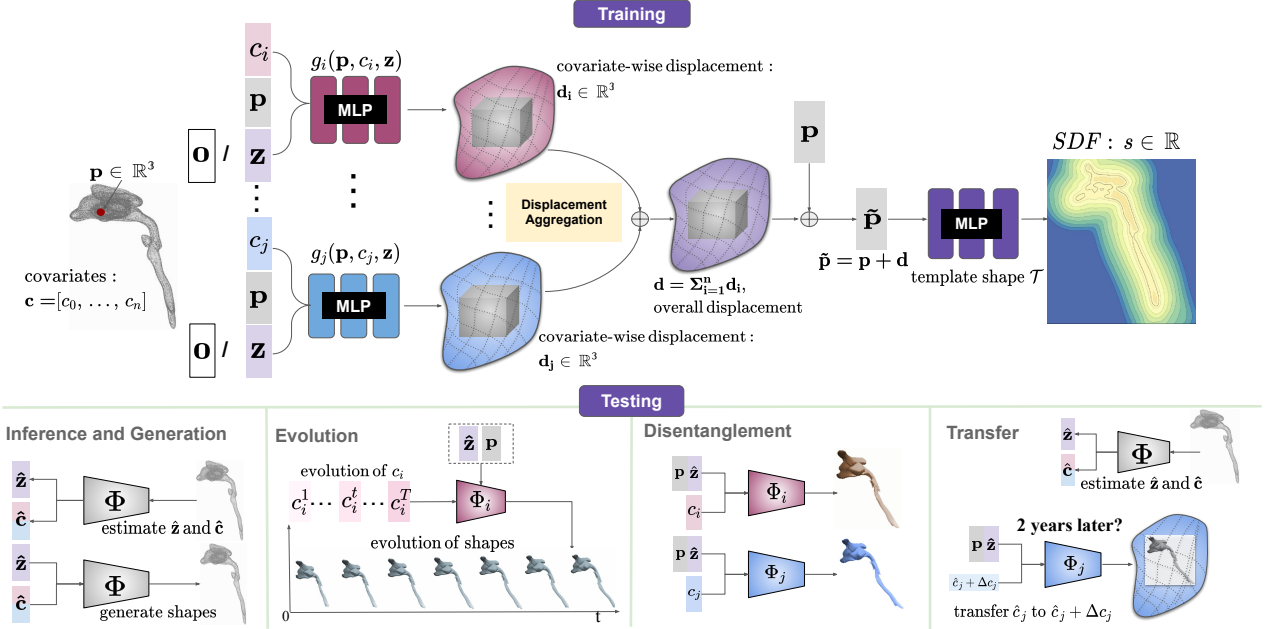


Figure 1. Neural Additive Implicit Shape Representation. During training we learn the template \mathcal{T} and the neural networks $\{g_i\}$ predicting the covariate-wise displacement fields $\{d_i\}$. The displacement fields are added to obtain the overall displacement field \mathbf{d} defined in the target space; \mathbf{d} provides the displacement between the deformed template shape \mathcal{T} and the target shape that is to be captured. Specifically the template shape is queried not at its original coordinates \mathbf{p} , but instead at $\tilde{\mathbf{p}} = \mathbf{p} + \mathbf{d}$ effectively spatially deforming the template. At test time we evaluate the trained multi-layer perceptrons (MLPs) to use them for shape reconstruction, evolution, disentanglement, and shape transfer.

directly observed may be due to individual shape variation, unknown or missing covariates, or variations due to differences in data acquisition or data preprocessing errors. We capture these not directly observed factors by a latent code \mathbf{z} . The covariates \mathbf{c} and the latent code \mathbf{z} then contribute jointly to the displacement \mathcal{D} with respect to the template shape \mathcal{T} .

Inspired by neural additive [2] and generalized additive [20] models, we assume the overall displacement field is the sum of displacement fields that are controlled by individual covariates: $\mathcal{D} = \sum_i \mathcal{D}_i$. Here, \mathcal{D}_i is the displacement field controlled by the i -th covariate, c_i . This results by construction in an overall displacement \mathcal{D} that is disentangled into several sub-displacement fields $\{\mathcal{D}_i\}$. Conversely, the sub-displacement field $\{\mathcal{D}_i\}$ controlled by the covariates \mathbf{c} jointly determine the overall displacement \mathcal{D} .

3.2. Model Formulation

Fig. 1 gives an overview of NAISR. To obtain a continuous atlas representation, we use DIFs to represent both the template \mathcal{T} and the displacement field \mathcal{D} . The template shape \mathcal{T} is represented by a signed distance function, where the zero level set $\{\mathbf{p} \in \mathbb{R}^3 | \mathcal{T}(\mathbf{p}) = 0\}$ captures the desired template shape. The displacement \mathcal{D}_i of a particular point \mathbf{p} can also be represented implicitly as $\mathbf{d}_i = f_i(\mathbf{p}, c_i, \mathbf{z}) \in \mathbb{R}^3$. We use SIREN [44] as the backbone for $\mathcal{T}(\cdot)$ and $\{f_i(\cdot)\}$. Considering that the not directly observed factors might influence the geometry of all covariate-specific networks, we

make the latent code, \mathbf{z} , visible to all subnetworks $\{f_i(\cdot)\}$. We normalize the covariates so that they are centered at zero. To assure that a zero covariate value results in a zero displacement we parameterize the displacement fields as $\mathbf{d}_i = g_i(\mathbf{p}, c_i, 0, \mathbf{z})$ where

$$g_i(\mathbf{p}, x, y, \mathbf{z}) = f_i(\mathbf{p}, x, \mathbf{z}) - f_i(\mathbf{p}, y, \mathbf{z}). \quad (1)$$

The sub-displacement fields are added to obtain the overall displacement field

$$\mathbf{d} = g(\mathbf{p}, \mathbf{c}, \mathbf{z}) = \sum_{i=1}^N g_i(\mathbf{p}, c_i, 0, \mathbf{z}). \quad (2)$$

Based on this displacement field we deform the template shape \mathcal{T} to obtain an implicit representation of a target shape

$$s = \Phi(\mathbf{p}, \mathbf{c}, \mathbf{z}) = \mathcal{T}(\tilde{\mathbf{p}}) = \mathcal{T}(\mathbf{p} + \sum_{i=1}^N g_i(\mathbf{p}, c_i, \mathbf{z})), \quad (3)$$

where \mathbf{p} is a point in the source shape space, e.g., a point on the surface of shape \mathcal{S}_i and $\tilde{\mathbf{p}}$ represents a point in the template shape space, e.g., a point on the surface of the template shape \mathcal{T} . To investigate how an individual covariate c_i affects a shape we can simply extract the zero level set of

$$s_i = \Phi_i(\mathbf{p}, c_i, \mathbf{z}) = \mathcal{T}(\mathbf{p} + \mathbf{d}_i) = \mathcal{T}(\mathbf{p} + g_i(\mathbf{p}, c_i, \mathbf{z})). \quad (4)$$

3.3. Training

Training Strategy We use the zero-padding strategy of [24, 27] to minimize the influence of the latent code \mathbf{z} on shape differences that should be explained by the covariates \mathbf{c} . By also setting \mathbf{z} to $\mathbf{0}$ while optimizing the objective function, the model is pushed to rely on \mathbf{c} as much as possible.

Losses All our losses are ultimately summed over all shapes of the training population with the appropriate covariates \mathbf{c}_k and shape code \mathbf{z}_k for each shape \mathcal{S}^k . For ease of notation, we describe them for individual shapes in the following. For each shape, we sample on-surface and off-surface points. On-surface points have zero signed distance values and normal vectors extracted from the gold standard¹ mesh. Off-surface points have non-zero signed distance values but no normal vectors. Our losses for reconstruction follow [44, 33]. For points on the surface, the losses are

$$\begin{aligned} \mathcal{L}_{\text{on}}(\Phi, \mathbf{c}, \mathbf{z}) = & \int_{\mathcal{S}} \lambda_1 \underbrace{\|\|\nabla_{\mathbf{p}}\Phi(\mathbf{p}, \mathbf{c}, \mathbf{z})\| - 1\|}_{\mathcal{L}_{\text{Eikonal}}} \\ & + \lambda_2 \underbrace{\|\Phi(\mathbf{p}, \mathbf{c}, \mathbf{z})\|}_{\mathcal{L}_{\text{Dirichlet}}} + \lambda_3 \underbrace{(1 - \langle \nabla_{\mathbf{p}}\Phi(\mathbf{p}, \mathbf{c}, \mathbf{z}), \mathbf{n}(\mathbf{p}) \rangle)}_{\mathcal{L}_{\text{Neumann}}} d\mathbf{p}, \end{aligned} \quad (5)$$

where $\mathbf{n}(\mathbf{p})$ is the normal vector at \mathbf{p} and $\langle \cdot \rangle$ denotes the cosine similarity. For points off the surface, we use

$$\begin{aligned} \mathcal{L}_{\text{off}}(\Phi, \mathbf{c}, \mathbf{z}) = & \int_{\Omega \setminus \mathcal{S}} \lambda_4 \underbrace{\|\Phi(\mathbf{p}, \mathbf{c}, \mathbf{z}) - s_{tgt}(\mathbf{p})\|}_{\mathcal{L}_{\text{Dirichlet}}} \\ & + \lambda_5 \underbrace{\|\|\nabla_{\mathbf{p}}\Phi(\mathbf{p}, \mathbf{c}, \mathbf{z})\| - 1\|}_{\mathcal{L}_{\text{Eikonal}}} d\mathbf{p}, \end{aligned} \quad (6)$$

where $s_{tgt}(\mathbf{p})$ is the signed distance value at \mathbf{p} corresponding to a given target shape. Similar to [37, 31] we penalize the squared L^2 norm of the latent code \mathbf{z} as

$$\mathcal{L}_{\text{lat}}(\mathbf{z}) = \lambda_6 \frac{1}{\sigma^2} \|\mathbf{z}\|_2^2. \quad (7)$$

Further, we use an approximate inverse consistency loss [17, 49] to regularize the displacement fields. The basic idea is that the approximate inverse transformation $g_i^{-1}(\cdot)$ of $g_i(\cdot)$ should be able to map a point in the template space back to the point in the source space where

$$\begin{aligned} g_i^{-1}(\tilde{\mathbf{p}}) &= g_i(\mathbf{p} + \mathbf{d}_i, 0, c_i, \mathbf{z}) \\ &= f_i(\mathbf{p} + \mathbf{d}_i, 0, \mathbf{z}) - f_i(\mathbf{p} + \mathbf{d}_i, c_i, \mathbf{z}). \end{aligned} \quad (8)$$

The inverse consistency loss can then be written as

$$\mathcal{L}_{\text{inv}}(\{g_i\}, \mathbf{z}) = \lambda_7 \int_{\mathcal{S}} \sum_{i=1}^N \|(-\mathbf{d}_i) - g_i^{-1}(\mathbf{p} + \mathbf{d}_i)\| d\mathbf{p}. \quad (9)$$

¹In medical imaging, there is typically no groundtruth. We use *gold standard* to indicate shapes based off of manual or automatic segmentations, which are our targets for shape reconstruction.

As a result, our overall loss (for a given shape) is

$$\begin{aligned} \mathcal{L}(\Phi, \{g_i\}, \mathbf{c}, \mathbf{z}) = & \underbrace{\mathcal{L}_{\text{lat}}(\mathbf{z})}_{\mathcal{L}_{\text{latent_space}}} \\ & + \underbrace{\mathcal{L}_{\text{on}}(\Phi, \mathbf{c}, \mathbf{z}) + \mathcal{L}_{\text{off}}(\Phi, \mathbf{c}, \mathbf{z}) + \mathcal{L}_{\text{inv}}(\{g_i\}, \mathbf{z})}_{\mathcal{L}_{\text{reconstruction}}} \\ & + \underbrace{\mathcal{L}_{\text{on}}(\Phi, \mathbf{c}, \mathbf{0}) + \mathcal{L}_{\text{off}}(\Phi, \mathbf{c}, \mathbf{0}) + \mathcal{L}_{\text{inv}}(\{g_i\}, \mathbf{0})}_{\mathcal{L}_{\text{zero_padding}}}, \end{aligned} \quad (10)$$

where the parameters of Φ , $\{g_i\}$, and \mathbf{z} are trainable.

3.4. Testing

As shown in Fig. 1, our proposed NAISR is designed to accomplish the following tasks: shape reconstruction, shape disentanglement, shape evolution, and shape transfer. Further, NAISR also allows for shape interpolation, shape completion, and shape correspondence by design as [69, 46].

Shape Reconstruction and Generation As illustrated in the inference section in Fig. 1, a shape s_{tgt} is given and the goal is to recover its corresponding latent code \mathbf{z} and the covariates \mathbf{c} . To estimate these quantities, the network parameters stay fixed and we optimize over the covariates \mathbf{c} and the latent code \mathbf{z} which are both randomly initialized [37, 31]. Specifically, we solve the optimization problem

$$\hat{\mathbf{c}}, \hat{\mathbf{z}} = \arg \min_{\mathbf{c}, \mathbf{z}} \mathcal{L}(\Phi, \mathbf{c}, \mathbf{z}). \quad (11)$$

In clinical scenarios, the covariates \mathbf{c} might be known (e.g., recorded age or weight at imaging time). In this case, we only infer the latent code \mathbf{z} by the optimization

$$\hat{\mathbf{z}} = \arg \min_{\mathbf{z}} \mathcal{L}(\Phi, \mathbf{c}, \mathbf{z}). \quad (12)$$

A new shape of a patient with only the covariates altered can be generated by extracting the zero level set of $\Phi(\mathbf{p}, \mathbf{c}_{\text{new}}, \hat{\mathbf{z}})$.

Shape Evolution Shape evolution along covariates $\{c_i\}$ is desirable in shape analysis to obtain knowledge of disease progression or population trends in the shape population \mathcal{S} . For a time-varying covariate $(c_i^0, \dots, c_i^t, \dots, c_i^T)$, we obtain the corresponding shape evolution by $(\Phi_i(\mathbf{p}, c_i^0, \hat{\mathbf{z}}), \dots, \Phi_i(\mathbf{p}, c_i^t, \hat{\mathbf{z}}), \dots, \Phi_i(\mathbf{p}, c_i^T, \hat{\mathbf{z}}))$. If some covariates are correlated (e.g., age and weight), we can first obtain a reasonable evolution of the covariates $(\mathbf{c}^0, \dots, \mathbf{c}^t, \dots, \mathbf{c}^T)$ and the corresponding shape evolution as $(\Phi(\mathbf{p}, \mathbf{c}^0, \hat{\mathbf{z}}), \dots, \Phi(\mathbf{p}, \mathbf{c}^t, \hat{\mathbf{z}}), \dots, \Phi(\mathbf{p}, \mathbf{c}^T, \hat{\mathbf{z}}))$.

Shape Disentanglement As shown in the disentanglement section in Fig. 1, the displacement for a particular covariate c_i displaces point \mathbf{p} in the source space to $\mathbf{p} + \mathbf{d}_i$

in the template space for a given or inferred $\hat{\mathbf{z}}$ and c_i . We obtain the corresponding implicit signed distance field as

$$s_i = \Phi_i(\mathbf{p}, c_i, \hat{\mathbf{z}}) = \mathcal{T}(\mathbf{p} + \mathbf{d}_i) = \mathcal{T}(\mathbf{p} + g_i(\mathbf{p}, c_i, \hat{\mathbf{z}})). \quad (13)$$

As a result, the zero level sets of $\{\Phi_i(\cdot)\}$ represent shapes warped by the sub-displacement fields controlled by c_i .

Shape Transfer We use the following clinical scenario to introduce the shape transfer task. Suppose a doctor has conducted simulated surgery on an airway shape with the goal of previewing treatment effects on the shape after a period of time. This question can be answered by our shape transfer approach. Specifically, as shown in the transfer section in Fig. 1, after obtaining the inferred latent code $\hat{\mathbf{z}}$ and covariates $\hat{\mathbf{c}}$ from reconstruction, one can transfer the shape from the current covariates $\hat{\mathbf{c}}$ to new covariates $\hat{\mathbf{c}} + \Delta\mathbf{c}$ with $\Phi(\mathbf{p}, \hat{\mathbf{c}} + \Delta\mathbf{c}, \hat{\mathbf{z}})$. As a result, the transferred shape is a prediction of the outcome of the simulated surgery; it is the zero level set of $\Phi(\mathbf{p}, \hat{\mathbf{c}} + \Delta\mathbf{c}, \hat{\mathbf{z}})$. In more general scenarios, the covariates are unavailable but it is possible to infer them from the measured shapes themselves (see Eqs. (11)-(12)). Therefore, in shape transfer we are not only evolving a shape, but may also first estimate the initial state to be evolved.

4. Experiments

We evaluate NAISR in terms of shape reconstruction, shape disentanglement, shape evolution, and shape transfer. We can quantitatively evaluate NAISR for shape reconstruction and shape transfer because our dataset contains longitudinal observations. For shape evolution and shape disentanglement, we provide visualizations of covariate extrapolations to demonstrate that our method is capable of learning a reasonable representation of the deformations governed by the covariates. More details of the dataset and the experiments are available in the supplementary material.

Dataset. We use a pediatric airway dataset containing 357 airway shapes to evaluate our method. These airway shapes are obtained from automatic airway segmentations of computed tomography (CT) images of the upper airway of children with a radiographically normal airway. These 357 airway shape are from 263 patients, 34 of whom have longitudinal observations and 229 of whom have only been observed once. We use a 80%-20% train-test split by patient (instead of shapes); i.e., a given patient cannot simultaneously be in the train and the test set and therefore no information can leak between these two sets. Each shape has 3 covariates (age, weight, sex) and 11 annotated anatomical landmarks. Errors in the shapes $\{\mathcal{S}^k\}$ may arise from image segmentation error, differences in head positioning, missing parts of the airway shapes due to incomplete image coverage, and dynamic airway deformations due to breathing.

Data Processing The shape meshes are extracted using Marching Cubes [25, 51] to obtain coordinates and normal vectors of on-surface points. The airway shapes are rigidly aligned using the anatomical landmarks. The true vocal cords landmark is set to the origin. We follow the implementation in [37] to sample 500,000 off-surface points. During training, it is important to preserve the scale information. We therefore scale all meshes with the same constant.

Comparison Methods For shape reconstruction of unseen shapes, we compare our method on the test set with DeepSDF [37] A-SDF [31] DIT [69] and NDF [46]. For shape transfer, we compare our method with A-SDF [31] because other comparison methods cannot model covariates as summarized in Tab. 1. The original implementations of the comparison methods did not produce satisfying reconstructions on our dataset. We therefore improved them by using our reconstruction losses and by using the SIREN backbone [44] in DeepSDF [37], A-SDF [31], and the template networks in DIT [69] and NDF [46].

Metrics For evaluation, all target shapes and reconstructed meshes are normalized to a unit sphere as in [37] to assure that large shapes and small shapes contribute equally to error measurements. We use the Hausdorff distance, Chamfer distance, and earth mover’s distance to evaluate the performance of our shape reconstructions. We also report the number of model parameters. For shape transfer, considering that a perfectly consistent image acquisition process is impossible for different observations (e.g., head positioning might slightly vary across timepoints), we visualize the transferred shapes and evaluate based on the difference between the *volumes* of the reconstructed shapes and the target shapes.

4.1. Shape Reconstruction

The goal of our shape reconstruction experiment is to demonstrate that NAISR can provide competitive reconstruction performance while providing interpretability. Tab. 2 shows the quantitative evaluations. Fig. 2 visualizes reconstructed shapes. We observe that implicit shape representations can complete missing shape parts which can benefit further shape analysis. DeepSDF [37] performs better than the deformation-based methods [43, 69], likely because it directly optimizes individual shape reconstructions instead of relying on the deformations of a template shape. A-SDF [31] works well for representing shapes in the training set but cannot reconstruct unseen shapes successfully. The reason might be small amount of available longitudinal data, with A-SDF memorizing each shape and its covariates instead of learning to infer how the covariates affect shapes in general.

Methods	Deformable	# params	CD mean	CD median	EMD mean	EMD median	HD mean	HD median
DeepSDF [37]	✗	2.24M	0.143	0.023	1.249	0.991	9.860	6.750
DIT [69]	✓	3.70M	0.061	0.032	1.135	1.032	10.528	8.192
NDF [46]	✓	0.34M	0.091	0.056	1.461	1.371	12.110	9.986
A-SDF [31] (with Cov.)	✗	1.98M	0.658	0.083	3.028	1.744	26.678	18.623
A-SDF [31]	✗	1.98M	0.412	0.097	2.900	2.023	24.266	16.755
NAISR (with Cov.)	✓	2.33M	0.059	0.031	1.200	1.109	10.334	8.287
NAISR	✓	2.33M	0.056	0.030	1.165	1.061	9.968	8.104

Table 2. Quantitative evaluation of shape reconstruction. CD = Chamfer distance. EMD = Earth mover’s distance. HD = Hausdorff distance. All metrics are multiplied by 10^2 . Bold red values indicate the best scores across all methods. Bold black values indicate the 2nd best scores of all methods. **NAISR (with Cov.)** means the covariates are used as input during inference (see Eq. (12)). **NAISR** means the covariates were inferred during testing (see Eq. (11)). **NAISR** performs well for reconstruction allowing for interpretability.

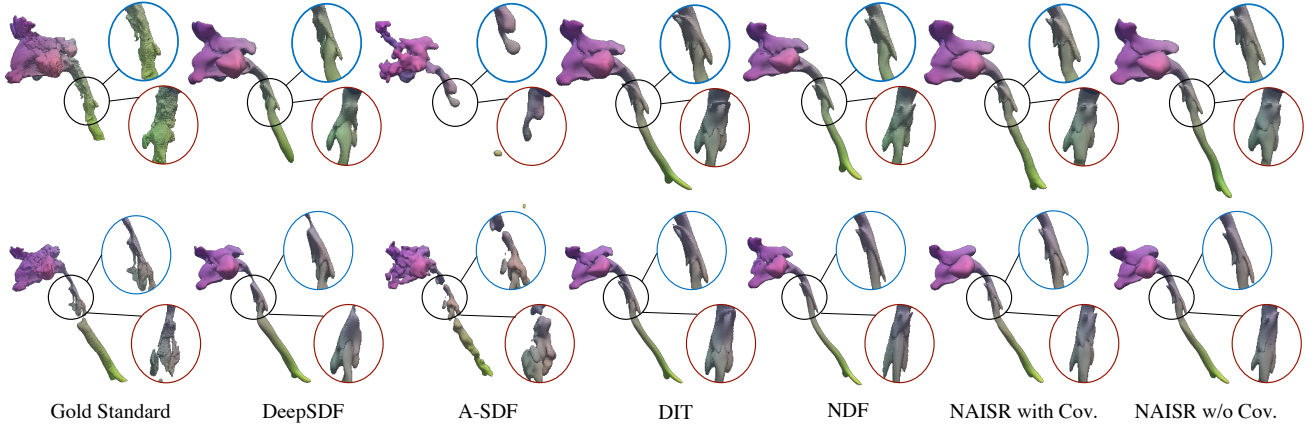


Figure 2. Visualizations of shape reconstructions with different methods. The red and blue circles show the structure in the black circle from two different views. **NAISR** can produce detailed and accurate reconstructions as well as impute missing airway parts.

4.2. Shape Transfer

The goal of our shape transfer experiment is to evaluate NAISR’s ability to transfer a shape \mathcal{S}^0 from the current covariates \mathbf{c}^0 (which might be unknown) to different covariates \mathbf{c}^t . We use the longitudinal data in the dataset for evaluation. Specifically, we treat the earliest shape observation of a patient as the current shape \mathcal{S}^0 and attempt to transfer \mathcal{S}^0 from \mathbf{c}^0 to \mathbf{c}^t to capture the later shape \mathcal{S}^t .

First, we obtain the inferred latent code $\hat{\mathbf{z}}$ and covariates $\hat{\mathbf{c}}^0$ of \mathcal{S}^0 by reconstruction. Then, we transfer \mathcal{S}^0 to \mathcal{S}^t with $\Phi(\mathbf{p}, \hat{\mathbf{c}}^0 + \Delta\mathbf{c}, \hat{\mathbf{z}})$ by setting $\Delta\mathbf{c}$ to $\mathbf{c}^t - \mathbf{c}^0$, where \mathbf{c}^t and \mathbf{c}^0 are the covariates of the longitudinal data. Ideally, the inferred $\hat{\mathbf{c}}^0$ is exactly \mathbf{c}^0 . The zero level set of $\Phi(\mathbf{p}, \hat{\mathbf{c}}^0 + \Delta\mathbf{c}, \hat{\mathbf{z}})$ is then the transferred shape and it is evaluated by comparing it with the gold standard shape \mathcal{S}^t .

Tab. 3 shows a shape transfer example for a cancer patient who was scanned 11 times. We observe that our method can produce transferred shapes that correspond well with the measured shapes. Further, we are able to infer *complete* shapes. Fig. 3 shows quantitative results for the volume

differences between our transferred shapes and the gold standard shapes. Our method performs best. Our results demonstrate that NAISR is capable of transferring shapes to other timepoints \mathcal{S}^t from a given initial state \mathcal{S}^0 .

4.3. Shape Disentanglement and Evolution

Fig. 4 shows that NAISR is able to extrapolate reasonable shapes changes when varying age and weight. These results illustrate the capabilities of NAISR for shape disentanglement and to capture shape evolutions. Note that when evolving shapes along one covariate c_i , the deformations from other covariates are naturally set to 0 by our model construction (see Sec. 3.2). As a result, the shapes in the yellow and green boxes in Figure 4 represent the disentangled shape evolutions along age and weight respectively. The shapes in the other grid positions can be extrapolated using $\Phi(\cdot)$. By inspecting the volume changes along age and weight in Fig. 4, we observe that age is more important for airway volume than weight. These observations from our generated shapes are consistent with clinical expectations for pediatric airways [26], suggesting that NAISR is able to

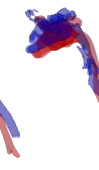
# time	0	1	2	3	4	5	6	7	8	9	10
$\{\mathcal{S}^t\}$											
# time	0	1	2	3	4	5	6	7	8	9	10
weight	55.20	60.90	64.30	65.25	59.25	59.20	65.30	68.00	77.10	75.60	75.60
age	154	155	157	159	163	164	167	170	194	227	233
sex	male	male	male	male							
p-vol	88.40	89.47	90.42	90.95	90.71	90.91	92.46	93.48	99.66	107.99	110.16
m-vol	86.33	82.66	63.23	90.65	98.11	84.35	94.14	127.45	98.81	100.17	113.84

Table 3. Shape transfer for a patient. Blue: gold standard shapes; red: transferred shapes with NAISR. The table below lists the covariates (age/month, weight/kg, sex) for the shapes above. P-vol(predicted volume) is the volume (cm^3) of the transferred shape by NAISR w/o covariates following Eq. (11). M-vol (measured volume) is the volume (cm^3) of the shapes based on the actual imaging. NAISR can capture the trend of growing volume with age and weight while producing clear, complete, and topology-consistent shapes.

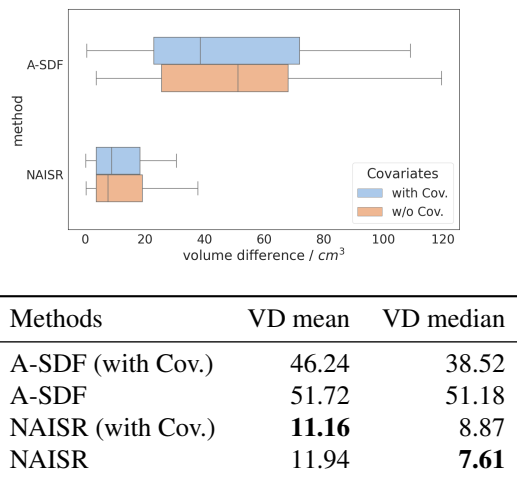


Figure 3. Statistics of Volume Difference (VD, cm^3) between transferred shapes and gold standard shapes. Bold scores indicate the best performance across all methods. The blue results in the boxplot represent the reconstruction step following Eq. (12). The orange results represent the reconstruction step following Eq. (11). NAISR results in significantly improved volume estimates.

extract hidden knowledge from data and is able to generate interpretable results directly as 3D shapes.

5. Limitations and Future Work

Invertible transformations are typically desirable for shape correspondence. However, our approach cannot guarantee invertibility. Invertibility could be guaranteed by representing deformations via velocity fields instead of directly parameterizing deformation fields. However, velocity field parameterizations are costly as they require numerical inte-

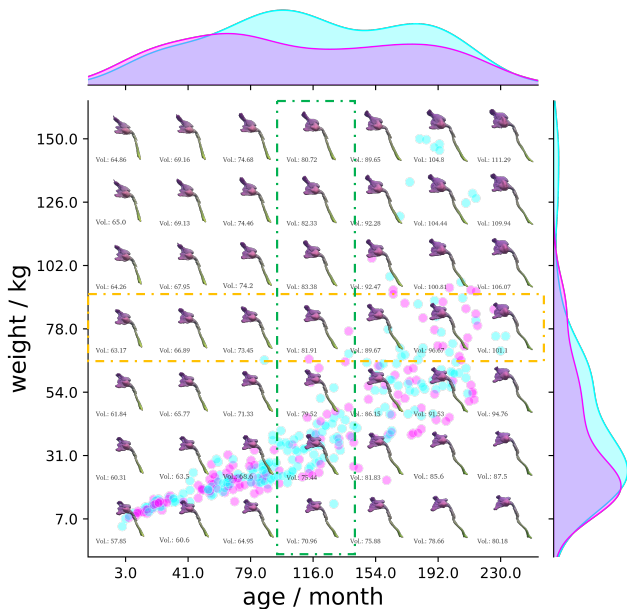


Figure 4. Shape extrapolation in covariate space. Example shapes in the age-weight space are visualized with their volumes (cm^3) below. Cyan points represent male and purple points female children in the dataset. The points represent the covariates of all children in the dataset. The colored shades represent the age and weight distributions stratified by sex. The latent code \mathbf{z} is kept constant to create an individualized covariate shape space. The shapes in the green and yellow boxes are plotted with $\{\Phi_i\}$ (see Sec. 3.4), representing the disentangled shape evolutions along weight and age respectively. (Best viewed zoomed.)

gration. Hence, training such velocity field models for implicit shapes would consume more time and GPU resources. In future work, we will develop more efficient invertible representations, which will then assure that shape topology

is preserved by construction. We also do not know the true effects of covariates on the shapes. We can so far only indirectly assess our model by quantifying reconstruction, evolution, and transfer performance. In the future, we will include patients with airway abnormalities (e.g., with subglottic stenosis, an airway disease affecting airway geometry) in our analyses. This would allow us to further assess our NAISR model by exploring if our estimated model of normal airway shape can be used to detect airway abnormalities.

6. Conclusion

In this work, we proposed NAISR, a 3D neural additive model for interpretable shape representation. Compared to other shape representation methods, NAISR 1) captures the effect of individual covariates on shapes; 2) can transfer shapes to new covariates, e.g., to infer anatomy development; and 3) can provide shapes based on extrapolated covariates. NAISR is the first approach combining deep implicit shape representations based on template deformation with the ability to account for covariates. Although our driving problem is to provide an atlas of the upper airway in children, our approach can be used for general interpretable shape representation and shape analysis.

References

- [1] Panos Achlioptas, Olga Diamanti, Ioannis Mitliagkas, and Leonidas Guibas. Learning representations and generative models for 3d point clouds. In *International conference on machine learning*, pages 40–49. PMLR, 2018. 1, 2
- [2] Rishabh Agarwal, Nicholas Frosst, Xuezhou Zhang, Rich Caruana, and Geoffrey E Hinton. Neural additive models: Interpretable machine learning with neural nets. *arXiv preprint arXiv:2004.13912*, 2020. 3, 4
- [3] Sercan Ö Arik and Tomas Pfister. Tabnet: Attentive interpretable tabular learning. In *Proceedings of the AAAI Conference on Artificial Intelligence*, volume 35, pages 6679–6687, 2021. 3
- [4] Cosmin I Bercea, Benedikt Wiestler, Daniel Rueckert, and Shadi Albarqouni. Federated disentangled representation learning for unsupervised brain anomaly detection. *Nature Machine Intelligence*, 4(8):685–695, 2022. 3
- [5] Jeroen Berrevoets, Ahmed Alaa, Zhaozhi Qian, James Jordon, Alexander ES Gimson, and Mihaela Van Der Schaar. Learning queueing policies for organ transplantation allocation using interpretable counterfactual survival analysis. In *International Conference on Machine Learning*, pages 792–802. PMLR, 2021. 3
- [6] Agisilaos Chartsias, Thomas Joyce, Giorgos Papanastasiou, Scott Semple, Michelle Williams, David E Newby, Rohan Dharmakumar, and Sotirios A Tsafaris. Disentangled representation learning in cardiac image analysis. *Medical image analysis*, 58:101535, 2019. 3
- [7] Kan Chen, Qishuo Yin, and Qi Long. Covariate-balancing-aware interpretable deep learning models for treatment effect estimation. *arXiv preprint arXiv:2203.03185*, 2022. 3
- [8] Xu Chen, Yufeng Zheng, Michael J Black, Otmar Hilliges, and Andreas Geiger. Snarf: Differentiable forward skinning for animating non-rigid neural implicit shapes. In *Proceedings of the IEEE/CVF International Conference on Computer Vision*, pages 11594–11604, 2021. 3
- [9] Jiebin Chu, Yaoyun Zhang, Fei Huang, Luo Si, Songfang Huang, and Zhengxing Huang. Disentangled representation for sequential treatment effect estimation. *Computer Methods and Programs in Biomedicine*, 226:107175, 2022. 3
- [10] Jonathan Crabbe, Zhaozhi Qian, Fergus Imrie, and Mihaela van der Schaar. Explaining latent representations with a corpus of examples. In M. Ranzato, A. Beygelzimer, Y. Dauphin, P.S. Liang, and J. Wortman Vaughan, editors, *Advances in Neural Information Processing Systems*, volume 34, pages 12154–12166. Curran Associates, Inc., 2021. 3
- [11] Adrian Dalca, Marianne Rakic, John Guttag, and Mert Sabuncu. Learning conditional deformable templates with convolutional networks. *Advances in neural information processing systems*, 32, 2019. 2, 3
- [12] Boyang Deng, John P Lewis, Timothy Jeruzalski, Gerard Pons-Moll, Geoffrey Hinton, Mohammad Norouzi, and Andrea Tagliasacchi. Nasa neural articulated shape approximation. In *Computer Vision—ECCV 2020: 16th European Conference, Glasgow, UK, August 23–28, 2020, Proceedings, Part VII 16*, pages 612–628. Springer, 2020. 3
- [13] Yu Deng, Jiaolong Yang, and Xin Tong. Deformed implicit field: Modeling 3d shapes with learned dense correspondence. In *Proceedings of the IEEE/CVF Conference on Computer Vision and Pattern Recognition*, pages 10286–10296, 2021. 1, 2, 3
- [14] Zheng Ding, Yifan Xu, Weijian Xu, Gaurav Parmar, Yang Yang, Max Welling, and Zhuowen Tu. Guided variational autoencoder for disentanglement learning. In *Proceedings of the IEEE/CVF conference on computer vision and pattern recognition*, pages 7920–7929, 2020. 3
- [15] Jun Gao, Tianchang Shen, Zian Wang, Wenzheng Chen, Kangxue Yin, Daiqing Li, Or Litany, Zan Gojcic, and Sanja Fidler. Get3d: A generative model of high quality 3d textured shapes learned from images. In *Advances In Neural Information Processing Systems*, 2022. 1, 2, 3
- [16] Daniele Grattarola and Pierre Vandergheynst. Generalised implicit neural representations. *arXiv preprint arXiv:2205.15674*, 2022. 1
- [17] Hastings Greer, Roland Kwitt, François-Xavier Vialard, and Marc Niethammer. ICON: Learning regular maps through inverse consistency. In *Proceedings of the IEEE/CVF International Conference on Computer Vision*, pages 3396–3405, 2021. 5, 13
- [18] Amos Gropp, Lior Yariv, Niv Haim, Matan Atzmon, and Yaron Lipman. Implicit geometric regularization for learning shapes. *arXiv preprint arXiv:2002.10099*, 2020. 2
- [19] Thibault Groueix, Matthew Fisher, Vladimir G Kim, Bryan C Russell, and Mathieu Aubry. A papier-mâché approach to learning 3d surface generation. In *Proceedings of the IEEE conference on computer vision and pattern recognition*, pages 216–224, 2018. 1, 2
- [20] Trevor J Hastie. *Generalized additive models*. Routledge, 2017. 3, 4
- [21] Vineet John, Lili Mou, Hareesh Bahuleyan, and Olga Vechtomova. Disentangled representation learning for non-parallel text style transfer. *arXiv preprint arXiv:1808.04339*, 2018. 3
- [22] Hyungsik Jung and Youngrook Oh. Towards better explanations of class activation mapping. In *Proceedings of the IEEE/CVF International Conference on Computer Vision*, pages 1336–1344, 2021. 3
- [23] Diederik P Kingma and Jimmy Ba. Adam: A method for stochastic optimization. *arXiv preprint arXiv:1412.6980*, 2014. 14
- [24] Xiang Li, Yasushi Makihara, Chi Xu, Yasushi Yagi, and Mingwu Ren. Gait recognition via semi-supervised disentangled representation learning to identity and covariate features. In *Proceedings of the IEEE/CVF Conference on Computer Vision and Pattern Recognition*, pages 13309–13319, 2020. 5
- [25] William E Lorensen and Harvey E Cline. Marching cubes: A high resolution 3d surface construction algorithm. *ACM siggraph computer graphics*, 21(4):163–169, 1987. 6
- [26] Romain Luscan, Nicolas Leboulanger, Pierre Fayoux, Gaspard Kerner, Kahina Belhous, Vincent Couloigner, Erea-Noël Garabedian, François Simon, Françoise Denoyelle, and Briac Thierry. Developmental changes of upper airway dimensions in children. *Pediatric Anesthesia*, 30(4):435–445, 2020. 7, 16
- [27] Ricardo Martin-Brualla, Noha Radwan, Mehdi S. M. Sajjadi, Jonathan T. Barron, Alexey Dosovitskiy, and Daniel

- Duckworth. NeRF in the Wild: Neural Radiance Fields for Unconstrained Photo Collections. In *CVPR*, 2021. 5
- [28] Roberto Martín-Martín, Clemens Eppner, and Oliver Brock. The rbo dataset of articulated objects and interactions. *The International Journal of Robotics Research*, 38(9):1013–1019, 2019. 15
- [29] Lars Mescheder, Michael Oechsle, Michael Niemeyer, Sebastian Nowozin, and Andreas Geiger. Occupancy networks: Learning 3d reconstruction in function space. In *Proceedings of the IEEE/CVF conference on computer vision and pattern recognition*, pages 4460–4470, 2019. 1
- [30] Raha Moraffah, Mansooreh Karami, Ruocheng Guo, Adrienne Raglin, and Huan Liu. Causal interpretability for machine learning-problems, methods and evaluation. *ACM SIGKDD Explorations Newsletter*, 22(1):18–33, 2020. 3
- [31] Jiteng Mu, Weichao Qiu, Adam Kortylewski, Alan Yuille, Nuno Vasconcelos, and Xiaolong Wang. A-sdf: Learning disentangled signed distance functions for articulated shape representation. In *Proceedings of the IEEE/CVF International Conference on Computer Vision*, pages 13001–13011, 2021. 2, 3, 5, 6, 7, 14, 15, 16
- [32] Michael Niemeyer, Lars Mescheder, Michael Oechsle, and Andreas Geiger. Occupancy flow: 4d reconstruction by learning particle dynamics. In *Proceedings of the IEEE/CVF international conference on computer vision*, pages 5379–5389, 2019. 2
- [33] Tiago Novello, Guilherme Schardong, Luiz Schirmer, Vinícius da Silva, Hélio Lopes, and Luiz Velho. Exploring differential geometry in neural implicits. *Computers & Graphics*, 108:49–60, 2022. 1, 5
- [34] Stanley Osher and Ronald P Fedkiw. *Level set methods and dynamic implicit surfaces*, volume 1. Springer New York, 2005. 2
- [35] Pablo Palafox, Aljaž Božič, Justus Thies, Matthias Nießner, and Angela Dai. Npms: Neural parametric models for 3d deformable shapes. In *Proceedings of the IEEE/CVF International Conference on Computer Vision*, pages 12695–12705, 2021. 3
- [36] Pablo Palafox, Nikolaos Sarafianos, Tony Tung, and Angela Dai. Spams: Structured implicit parametric models. In *Proceedings of the IEEE/CVF Conference on Computer Vision and Pattern Recognition*, pages 12851–12860, 2022. 1
- [37] Jeong Joon Park, Peter Florence, Julian Straub, Richard Newcombe, and Steven Lovegrove. DeepSDF: Learning continuous signed distance functions for shape representation. In *Proceedings of the IEEE/CVF conference on computer vision and pattern recognition*, pages 165–174, 2019. 1, 2, 3, 5, 6, 7, 14, 16
- [38] Pakkapon Phongthawee, Suttisak Wizadwongsa, Jiraphon Yenphraphai, and Supasorn Suwajanakorn. Nex360: Real-time all-around view synthesis with neural basis expansion. *IEEE Transactions on Pattern Analysis and Machine Intelligence*, 2022. 2
- [39] Marco Tulio Ribeiro, Sameer Singh, and Carlos Guestrin. "why should i trust you?" explaining the predictions of any classifier. In *Proceedings of the 22nd ACM SIGKDD international conference on knowledge discovery and data mining*, pages 1135–1144, 2016. 3
- [40] James Albert Sethian. *Level set methods and fast marching methods: evolving interfaces in computational geometry, fluid mechanics, computer vision, and materials science*, volume 3. Cambridge university press, 1999. 2
- [41] Tianchang Shen, Jun Gao, Kangxue Yin, Ming-Yu Liu, and Sanja Fidler. Deep marching tetrahedra: a hybrid representation for high-resolution 3d shape synthesis. *Advances in Neural Information Processing Systems*, 34:6087–6101, 2021. 2
- [42] Alon Shoshan, Nadav Bhonker, Igor Kviatkovsky, and Gerard Medioni. Gan-control: Explicitly controllable gans. In *Proceedings of the IEEE/CVF international conference on computer vision*, pages 14083–14093, 2021. 3
- [43] Anthony Simeonov, Yilun Du, Andrea Tagliasacchi, Joshua B. Tenenbaum, Alberto Rodriguez, Pulkit Agrawal, and Vincent Sitzmann. Neural descriptor fields: Se(3)-equivariant object representations for manipulation. *arXiv preprint arXiv:2112.05124*, 2021. 6, 16
- [44] Vincent Sitzmann, Julien Martel, Alexander Bergman, David Lindell, and Gordon Wetzstein. Implicit neural representations with periodic activation functions. *Advances in Neural Information Processing Systems*, 33:7462–7473, 2020. 1, 2, 4, 5, 6, 14
- [45] Wolfgang Stammer, Marius Memmel, Patrick Schramowski, and Kristian Kersting. Interactive disentanglement: Learning concepts by interacting with their prototype representations. In *Proceedings of the IEEE/CVF Conference on Computer Vision and Pattern Recognition*, pages 10317–10328, 2022. 3
- [46] Shanlin Sun, Kun Han, Deying Kong, Hao Tang, Xiangyi Yan, and Xiaohui Xie. Topology-preserving shape reconstruction and registration via neural diffeomorphic flow. In *Proceedings of the IEEE/CVF Conference on Computer Vision and Pattern Recognition*, pages 20845–20855, 2022. 1, 2, 3, 5, 6, 7
- [47] Ayush Tewari, Xingang Pan, Ohad Fried, Maneesh Agrawala, Christian Theobalt, et al. Disentangled3d: Learning a 3d generative model with disentangled geometry and appearance from monocular images. In *Proceedings of the IEEE/CVF Conference on Computer Vision and Pattern Recognition*, pages 1516–1525, 2022. 3
- [48] Jayaraman J Thiagarajan, Prasanna Sattigeri, Deepta Rajan, and Bindya Venkatesh. Calibrating healthcare ai: Towards reliable and interpretable deep predictive models. *arXiv preprint arXiv:2004.14480*, 2020. 3
- [49] Lin Tian, Hastings Greer, François-Xavier Vialard, Roland Kwitt, Raúl San José Estépar, and Marc Niethammer. GradICON: Approximate diffeomorphisms via gradient inverse consistency. In *Proceedings of the IEEE/CVF International Conference on Computer Vision*, 2023. 5, 13
- [50] Edgar Tretschk, Ayush Tewari, Vladislav Golyanik, Michael Zollhöfer, Carsten Stoll, and Christian Theobalt. Patchnets: Patch-based generalizable deep implicit 3d shape representations. In *Computer Vision—ECCV 2020: 16th European Conference, Glasgow, UK, August 23–28, 2020, Proceedings, Part XVI 16*, pages 293–309. Springer, 2020. 3
- [51] Stefan Van der Walt, Johannes L Schönberger, Juan Nunez-Iglesias, François Boulogne, Joshua D Warner, Neil Yager, Emmanuelle Gouillart, and Tony Yu. scikit-image: image processing in python. *PeerJ*, 2:e453, 2014. 6

- [52] Fangyin Wei, Rohan Chabra, Lingni Ma, Christoph Lassner, Michael Zollhoefer, Szymon Rusinkiewicz, Chris Sweeney, Richard Newcombe, and Mira Slavcheva. Self-supervised neural articulated shape and appearance models. In *Proceedings IEEE/CVF Conference on Computer Vision and Pattern Recognition (CVPR)*, 2022. 3
- [53] Chao Wen, Yinda Zhang, Zhuwen Li, and Yanwei Fu. Pixel2mesh++: Multi-view 3d mesh generation via deformation. In *Proceedings of the IEEE/CVF international conference on computer vision*, pages 1042–1051, 2019. 1, 2
- [54] Xin Wen, Junsheng Zhou, Yu-Shen Liu, Hua Su, Zhen Dong, and Zhizhong Han. 3d shape reconstruction from 2d images with disentangled attribute flow. In *Proceedings of the IEEE/CVF conference on computer vision and pattern recognition*, pages 3803–3813, 2022. 3
- [55] Jelmer M Wolterink, Jesse C Zwienenberg, and Christoph Brune. Implicit neural representations for deformable image registration. In *International Conference on Medical Imaging with Deep Learning*, pages 1349–1359. PMLR, 2022. 1
- [56] Sanghyun Woo, Jongchan Park, Joon-Young Lee, and In So Kweon. Cbam: Convolutional block attention module. In *Proceedings of the European conference on computer vision (ECCV)*, pages 3–19, 2018. 3
- [57] Jiajun Wu, Chengkai Zhang, Tianfan Xue, Bill Freeman, and Josh Tenenbaum. Learning a probabilistic latent space of object shapes via 3d generative-adversarial modeling. *Advances in neural information processing systems*, 29, 2016. 1, 2
- [58] Jiajun Wu, Chengkai Zhang, Xiuming Zhang, Zhoutong Zhang, William T Freeman, and Joshua B Tenenbaum. Learning shape priors for single-view 3d completion and reconstruction. In *Proceedings of the European Conference on Computer Vision (ECCV)*, pages 646–662, 2018. 1, 2
- [59] Zhirong Wu, Shuran Song, Aditya Khosla, Fisher Yu, Linguang Zhang, Xiaoou Tang, and Jianxiong Xiao. 3d shapenets: A deep representation for volumetric shapes. In *Proceedings of the IEEE conference on computer vision and pattern recognition*, pages 1912–1920, 2015. 1, 2
- [60] Mutian Xu, Junhao Zhang, Zhipeng Zhou, Mingye Xu, Xiaojuan Qi, and Yu Qiao. Learning geometry-disentangled representation for complementary understanding of 3d object point cloud. In *Proceedings of the AAAI Conference on Artificial Intelligence*, volume 35, pages 3056–3064, 2021. 3
- [61] Bangbang Yang, Chong Bao, Junyi Zeng, Hujun Bao, Yinda Zhang, Zhaopeng Cui, and Guofeng Zhang. Neumesh: Learning disentangled neural mesh-based implicit field for geometry and texture editing. In *Computer Vision–ECCV 2022: 17th European Conference, Tel Aviv, Israel, October 23–27, 2022, Proceedings, Part XVI*, pages 597–614. Springer, 2022. 1, 2, 3
- [62] Guandao Yang, Serge Belongie, Bharath Hariharan, and Vladlen Koltun. Geometry processing with neural fields. *Advances in Neural Information Processing Systems*, 34:22483–22497, 2021. 1
- [63] Jie Yang, Kaichun Mo, Yu-Kun Lai, Leonidas J Guibas, and Lin Gao. Dsm-net: Disentangled structured mesh net for controllable generation of fine geometry. *arXiv preprint arXiv:2008.05440*, 2(3), 2020. 3
- [64] Jiancheng Yang, Udaranga Wickramasinghe, Bingbing Ni, and Pascal Fua. Implicitatlas: learning deformable shape templates in medical imaging. In *Proceedings of the IEEE/CVF Conference on Computer Vision and Pattern Recognition*, pages 15861–15871, 2022. 2
- [65] Yaoqing Yang, Chen Feng, Yiru Shen, and Dong Tian. Foldingnet: Point cloud auto-encoder via deep grid deformation. In *Proceedings of the IEEE conference on computer vision and pattern recognition*, pages 206–215, 2018. 1, 2
- [66] Maciej Zamorski, Maciej Zięba, Piotr Klukowski, Rafał Nowak, Karol Kurach, Wojciech Stokowiec, and Tomasz Trzciański. Adversarial autoencoders for compact representations of 3d point clouds. *Computer Vision and Image Understanding*, 193:102921, 2020. 1, 2
- [67] Xiuming Zhang, Zhoutong Zhang, Chengkai Zhang, Josh Tenenbaum, Bill Freeman, and Jiajun Wu. Learning to reconstruct shapes from unseen classes. *Advances in neural information processing systems*, 31, 2018. 3
- [68] Yuting Zhang, Yijie Guo, Yixin Jin, Yijun Luo, Zhiyuan He, and Honglak Lee. Unsupervised discovery of object landmarks as structural representations. In *Proceedings of the IEEE Conference on Computer Vision and Pattern Recognition*, pages 2694–2703, 2018. 3
- [69] Zerong Zheng, Tao Yu, Qionghai Dai, and Yebin Liu. Deep implicit templates for 3d shape representation. In *Proceedings of the IEEE/CVF Conference on Computer Vision and Pattern Recognition*, pages 1429–1439, 2021. 1, 2, 3, 5, 6, 7, 16
- [70] Bolei Zhou, Aditya Khosla, Agata Lapedriza, Aude Oliva, and Antonio Torralba. Learning deep features for discriminative localization. In *Computer Vision and Pattern Recognition*, 2016. 3
- [71] Hao Zhu, Xinxin Zuo, Sen Wang, Xun Cao, and Ruigang Yang. Detailed human shape estimation from a single image by hierarchical mesh deformation. In *Proceedings of the IEEE/CVF conference on computer vision and pattern recognition*, pages 4491–4500, 2019. 1, 2

Supplementary Material for NAISR

This supplementary material provides additional model illustrations, implementation details, experimental results, and ablation studies.

A. Method

In this section, we investigate how the displacement field and inverse consistency loss [17, 49] of Eq. (9) work. \mathbf{z} is omitted in the derivations because it stays the same in every equation.

A.1. Velocity Field

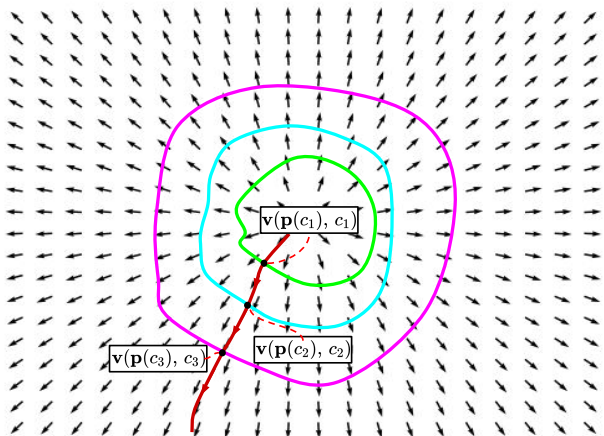


Figure 5. Velocity field. The velocity field $\mathbf{v}_i(\mathbf{p}(t), t)$ carries point \mathbf{p} from the green shape (at state c_1) to the cyan shape (at state c_2) and then to the purple shape (at state c_3) along the red trajectory. In our case, c_1 , c_2 and c_3 are different values of a covariate and $\mathbf{p}(c_1)$, $\mathbf{p}(c_2)$ and $\mathbf{p}(c_3)$ are points on shapes whose covariate values are c_1 , c_2 and c_3 respectively.

Suppose there is a velocity field $\mathbf{v}_i(\cdot)$ for each covariate c_i which can carry points to shapes with different values of the covariate c_i . As shown in Fig 5, the velocity field $\mathbf{v}_i(\cdot)$ carries the point $\mathbf{p}(c_1)$ from the green shape at c_1 to $\mathbf{p}(c_2)$ on the cyan shape at c_2 and then to $\mathbf{p}(c_3)$ on the purple shape at c_3 . Suppose the displacement field from source space to template space by covariate c_i can be represented by the integration of the velocity field $\mathbf{v}_i(\mathbf{p}(t), t)$, which is determined by the current point coordinate $\mathbf{p}(t)$ and current time t , as

$$\mathbf{d}_i = \mathbf{d}_{c_i \rightarrow 0}(\mathbf{p}(c_i)) = \int_{c_i}^0 \mathbf{v}_i(\mathbf{p}(t), t) dt, \quad (14)$$

where $\mathbf{d}_i = \mathbf{d}_{c_i \rightarrow 0}(\mathbf{p}(c_i))$ represents the displacement to transform point $\mathbf{p}(c_i)$ from source space (c_i) to template space (0). As illustrated Sec. 3.2, $g_i(\cdot)$ captures the displacement \mathbf{d}_i between spaces (e.g., source space to template space) by

$$\mathbf{d}_i = \mathbf{d}_{c_i \rightarrow 0}(\mathbf{p}(c_i)) = g_{c_i \rightarrow 0}(\mathbf{p}(c_i)) = g_i(\mathbf{p}(c_i), c_i, 0). \quad (15)$$

The inverse displacement from $\mathbf{p}(0)$ on template space (0) to source space (c_i) is

$$\begin{aligned} \mathbf{d}_i^{inv} &= g_{0 \rightarrow c_i}(\mathbf{p}(0)) = g_i(\mathbf{p}(0), 0, c_i) \\ &= \int_0^{c_i} \mathbf{v}_i(\mathbf{p}(t), t) dt. \end{aligned} \quad (16)$$

Therefore, a velocity field should allow for

$$\mathbf{d}_i = -\mathbf{d}_i^{inv} = -g_i(\mathbf{p}(0), 0, c_i). \quad (17)$$

Considering that $\mathbf{p}(0) = \mathbf{d}_i + \mathbf{p}(c_i)$, we can use the inverse consistency loss [17, 49] of Eq. (18) for the displacements $\{g_i(\cdot)\}$ to encourage g_i to be compatible with the requirements for integrating an underlying velocity field \mathbf{v}_i .

$$\mathcal{L}_{inv}(\{g_i\}) = \lambda_7 \int_{\mathcal{S}} \sum_{i=1}^N \|(-\mathbf{d}_i) - g_{0 \rightarrow c_i}(\mathbf{p} + \mathbf{d}_i)\| d\mathbf{p}. \quad (18)$$

B. Dataset

Our dataset includes 229 cross-sectional observations (where a patient was only imaged once) and 34 longitudinal observations. Tab. 4 shows the distribution of the number of observations across patients. Most patients in the dataset only have one observation; only 22 patients have ≥ 3 observation times. Tab. 5 shows the airway shapes and the demographic information of an example patient. Tab. 6 and Tab. 7 show the shapes and demographic information at different age percentiles for the whole data set and training set respectively. The time span of the training set is close but slightly smaller than the whole dataset. We observe that the time span of our longitudinal data for each patient is far shorter than the time span across the entire dataset, indicating the challenge of capturing spatiotemporal dependencies over large time spans between shapes while accounting for individual differences between patients.

# observations	1	2	3	4	5	6	7	9	11
# patients	229	12	6	8	3	2	1	1	1

Table 4. Number of patients for a given number of observations. For example, the 1st column indicates that there are 229 patients who were only observed once.

C. Experiments

Sec. C.1 describes implementation details. Sec. C.2, C.3, and C.4 show additional experimental results for shape reconstruction, shape transfer, and disentangled shape evolution respectively.

# time	0	1	2	3	4	5	6	7	8
# time	0	1	2	3	4	5	6	7	8
age	84.00	85.00	87.00	91.0	95.00	98.00	101.00	104.00	120.00
weight	20.40	20.40	21.00	21.9	22.80	22.90	23.50	24.90	28.50
sex	male	male	male	male	male	male	male	male	male
m-vol	30.07	32.18	48.95	33.8	44.87	42.29	28.42	40.92	61.36

Table 5. Visualization and demographic information of observations of a patient in our 3D airway shape dataset. Shapes are plotted with their covariates (age/month, weight/kg, sex) printed in the table. M-vol (measured volume) is the volume (cm^3) of the gold standard shapes based on the actual imaging.

P-	0	10	20	30	40	50	60	70	80	90	100
P-	0	10	20	30	40	50	60	70	80	90	100
age	1.00	23.00	55.00	71.00	89.00	111.00	129.00	161.00	179.00	199.00	233.00
weight	3.90	14.20	20.10	21.80	19.70	32.85	44.80	21.30	59.00	93.90	75.60
sex	male	male	female	female	male	male	male	female	female	female	male
m-vol	4.56	16.84	29.53	28.91	27.31	70.90	71.23	43.34	78.63	102.35	113.84

Table 6. Visualization and demographic information of our 3D airway shape dataset. Shapes of $\{0, 10, 20, 30, 40, 50, 60, 70, 80, 90, 100\}$ -th age percentiles are plotted with their covariates (age/month, weight/kg, sex) printed in the table. M-vol (measured volume) is the volume (cm^3) of the gold standard shapes based on the actual imaging.

C.1. Implementation Details

Each subnetwork, including the template network \mathcal{T} and the displacement networks $\{g_i\}$, are all parameterized with an 8-layer MLP using *sine* activations. The network parameter initialization follows SIREN [44]. There are 256 hidden units in each layer. The architecture of \mathcal{T} follows SIREN [44]. The architecture of the $\{g_i\}$ follows DeepSDF [37], in which a skip connection is used to concatenate the input of (\mathbf{p}, c_i) to the input of the middle layer. We use a latent code \mathbf{z} of dimension 256 ($L = 256$).

For each training iteration, the number of points sampled from each shape is 750 ($N = 750$), of which 500 are on-surface points ($N_{on} = 500$) and the others are off-surface points ($N_{off} = 250$). We train NAISR for 3000 epochs using Adam [23] with a learning rate $5e - 5$ and batch size of 64. Also, we jointly optimize the latent code \mathbf{z} with NAISR using Adam [23] with a learning rate of $1e - 3$.

During training, the hyperparameters in $\mathcal{L}_{reconstruction}$

and $\mathcal{L}_{zero_padding}$ are the same. In $\mathcal{L}_{reconstruction}$, $\lambda_1 = \lambda_5 = \frac{100}{N}$; $\lambda_2 = \frac{300}{N_{on}}$; $\lambda_3 = \frac{100}{N_{on}}$, $\lambda_4 = \frac{1000}{N_{off}}$. For \mathcal{L}_{lat} , $\lambda_6 = \frac{2e-4}{L}$; $\sigma = 0.01$ (following DeepSDF [37]). For \mathcal{L}_{inv} , $\lambda_7 = \frac{10}{N_{on}}$. During inference, the latent codes are optimized for 800 iterations with a learning rate of $5e - 3$. $\mathcal{L}_{zero_padding}$ is not used when the covariates are given as input as described by Eq. (12).

C.2. Shape Reconstruction

Tab. 8 shows the reconstruction performance of different methods for shapes in the training set. We can see that DeepSDF [37] and A-SDF [31] perform much better than other methods on the training set. The deformable methods perform similarly on the training set to the testing set. The non-deformable methods perform better on the training set than on the testing set. For example, A-SDF [31] performs exceptionally well on the training set; however, it cannot generalize to the testing set. This is because our dataset

P-	0	10	20	30	40	50	60	70	80	90	100
$\{\mathcal{S}^t\}$											
P-	0	10	20	30	40	50	60	70	80	90	100
age	3.00	22.00	55.00	69.00	88.00	106.00	124.00	160.00	179.00	199.00	230.00
weight	6.75	12.05	20.10	13.30	26.70	32.70	42.00	48.80	59.00	93.90	70.10
sex	male	female	female	female	male	male	male	male	female	female	male
m-vol	9.40	18.80	29.53	37.96	33.98	73.66	40.72	133.84	78.63	102.35	123.31

Table 7. Visualization and demographic information of the training set. The time span of the training set is close but slightly smaller than for the entire dataset. Shapes of $\{0, 10, 20, 30, 40, 50, 60, 70, 80, 90, 100\}$ -th age percentiles of age are plotted with their covariates (age/month, weight/kg, sex) printed in the table. M-vol (measured volume) is the volume (cm^3) of the gold standard shapes based on the actual imaging.

is more challenging than the RBO dataset [28] used in A-SDF [31], in which sufficient longitudinal data is available for the network to learn the interactions between geometries and articulations.

C.3. Shape Transfer

Tab. 10 shows the transferred shapes using NAISR with covariates as input (following Eq. (12)). The predicted shapes from Eq. (11) and Eq. (12) are consistent in terms of appearance, volume and development tendency. Tab. 9 shows the transferred shapes from NAISR of another patient following Eq. (12) and Eq.(11) respectively.

C.4. Disentangled Shape Evolution

Fig. 6 shows another example of shape extrapolation in covariate space. Fig. 7 visualizes shape extrapolation of an average airway shape. Specifically, we randomly select 10 latent codes $\{z_i\}$ of airway shapes in the training set and take the average of them as,

$$\bar{z} = \frac{1}{10} \sum_{i=1}^{10} z_i. \quad (19)$$

By comparing Fig. 6 and Fig. 7, we observe that extrapolating shapes with an average latent code \bar{z} produces a larger range of shapes while extrapolating shapes with just one latent code z_i tends to produce less shape variation. This might be because a particular latent code z_i should preserve patient-specific information and thus should shrink the shape space by producing similar shapes in covariate space. While using an average latent code \bar{z} , the population trend dominates patient-specific information. As a result, the extrapolated shape space from \bar{z} is able to reflect the overall shape development tendency in the large population better; it corresponds better with the population shape development shown in Tab. 6. We also observe that shapes

extrapolated from a single latent code z_i look more realistic and smooth across covariates while \bar{z} sometimes produces noisy shapes, especially when extrapolating shapes in unseen covariate space. We will attempt to alleviate this problem by using an efficient invertible displacement field in our future work to encourage reasonable shape extrapolation in unseen covariate space.

D. Ablation Studies

In this section, we investigate how the zero padding strategy and the inverse consistency loss influence NAISR’s performance in terms of shape reconstruction performance and shape extrapolation.

D.1. Shape Reconstruction

Tab. 11 shows quantitative evaluation results for shape reconstruction on the testing set using NAISR with different settings. We observe that not providing covariates as input during the testing stage produces better reconstruction results. This might be because the missing covariates leave the network more freedom to estimate the latent code z . The reconstruction performs best when there are no regularizations (i.e. neither zero padding nor inverse consistency). However, when using the zero-padding strategy to encourage the interpretability of the network, the inverse consistency loss becomes helpful to better reconstruct shapes.

D.2. Shape Disentanglement and Evolution

Tab. 8 visualizes the shape extrapolation results from the latent code z_i for a patient using different training settings. We observe that NAISR is able to produce realistic shapes with all experiment settings. However, the network has difficulty evolving shapes along weight when the zero-padding strategy is not used; as shown in Fig. 8(b,d).

Methods	Deformable	# params	CD mean	CD median	EMD mean	EMD median	HD mean	HD median
DeepSDF [37]	✗	2.24M	0.021	0.017	0.941	0.907	6.503	5.710
A-SDF [31]	✗	1.98M	0.013	0.011	0.804	0.768	4.962	4.353
DIT [69]	✓	3.70M	0.056	0.038	1.162	1.095	10.426	9.422
NDF[43]	✓	0.34M	0.072	0.053	1.406	1.335	11.277	10.116
NAISR	✓	2.33M	0.053	0.042	1.288	1.241	9.925	8.940

Table 8. Comparison of reconstruction performance on the training set using different methods. The deformable methods perform similarly on the training set to the testing set. The non-deformable methods perform better on the training set than on the testing set (see Tab. 2 for shape reconstruction results on the testing set).

# time	0	1	2	3	# time	0	1	2	3
									
$\{S^t\}$					$\{S^t\}$				
# time	0	1	2	3	# time	0	1	2	3
weight	20.30	20.60	27.50	27.90	weight	20.30	20.60	27.50	27.90
age	62.00	65.00	89.00	94.00	age	62.00	65.00	89.00	94.00
sex	male	male	male	male	sex	male	male	male	male
p-vol	61.20	61.91	69.14	70.66	p-vol	61.94	62.31	66.17	66.80
m-vol	49.61	58.87	55.91	62.07	m-vol	49.61	58.87	55.91	62.07

Table 9. Another shape transfer example. Left: using **NAISR with Cov.** based on Eq. (12); right: using **NAISR w/o Cov.** based on Eq. (11). Blue: gold standard shapes; red: transferred shapes with **NAISR**. The table below lists the covariates (age/month, weight/kg, sex) for the shapes above. P-vol(predicted volume) is the volume (cm^3) of the transferred shape by **NAISR** with covariates following Eq. (12). M-vol (measured volume) is the volume (cm^3) of the shapes based on the actual imaging.

Tab. 7 visualizes the shape extrapolation results from the average latent code \bar{z} (from Eq. (19)) for an average airway shape. We can observe that all settings work well when extrapolating shapes near the template airway, and all settings are able to produce tiny shapes for baby airways. Also, all settings can evolve the airway shapes reasonably if there are enough data points in the covariate space, indicating that **NAISR** is able to capture the airway development tendency of the population. However, all settings may produce unrealistic airways for unseen covariates. For example, the shapes in the left corner and right corner in Fig.9(a,b,c,d) look unrealistic. Shapes in the left corner in Fig.9(a,b,c,d) are baby airways of high weight which do not exist in reality while shapes in the right corner do not belong to pediatric airways (age ≥ 216 months) and few cases with those covariates exist in the dataset.

From Fig. 9, we see that the zero-padding strategy is necessary for the network to learn correct knowledge from data. For example, when not using the zero-padding strategy, as illustrated in Fig. 9(b,d), the network tends to infer a large volume increase for a simple weight increase when the patient is already an adult. However, this is less likely to happen in clinical observation as age plays a more important

role [26].

# time	0	1	2	3	4	5	6	7	8	9	10
$\{S^t\}$											
# time	0	1	2	3	4	5	6	7	8	9	10
weight	55.20	60.90	64.30	65.25	59.25	59.20	65.30	68.00	77.10	75.60	75.60
age	154.00	155.00	157.00	159.00	163.00	164.00	167.00	170.00	194.00	227.00	233.00
sex	male	male	male	male	male						
p-vol	89.97	92.09	93.80	94.76	94.23	94.56	97.42	99.18	107.96	114.66	116.01
m-vol	86.33	82.66	63.23	90.65	98.11	84.35	94.14	127.45	98.81	100.17	113.84

Table 10. Shape transfer using covariates as input for the patient shown in the main text. Blue: gold standard shapes; red: transferred shapes with **NAISR**. The table below lists the covariates (age/month, weight/kg, sex) for the shapes above. P-vol(predicted volume) is the volume (cm^3) of the transferred shape by NAISR with covariates following Eq. (12). M-vol (measured volume) is the volume (cm^3) of the shapes based on the actual imaging. The predicted shapes from **NAISR with Cov.** looks consistent to the shapes from **NAISR w/o Cov.**

Methods	with Cov.	with I.C.	with Z.P.	CD mean	CD median	EMD mean	EMD median	HD mean	HD median
NAISR	✓	✓	✓	0.059	0.031	1.200	1.109	10.334	8.287
NAISR	✓	✗	✓	0.071	0.033	1.246	1.129	10.972	8.771
NAISR	✓	✓	✗	0.064	0.032	1.272	1.167	10.576	8.143
NAISR	✓	✗	✗	0.058	0.031	1.131	1.063	10.735	8.554
NAISR	✗	✓	✓	0.056	0.030	1.165	1.061	9.968	8.104
NAISR	✗	✗	✓	0.059	0.029	1.179	1.082	10.078	8.140
NAISR	✗	✓	✗	0.060	0.032	1.249	1.161	9.950	7.830
NAISR	✗	✗	✗	0.054	0.027	1.086	1.009	10.216	7.992

Table 11. Shape reconstruction performance for different experiment settings. With Cov. denotes that covariates are used as input as described in Eq. (12). With I.C. indicates that the inverse consistency loss is used. With Z.P. denotes that the zero-padding strategy is used. The reconstruction performs best when there are no regularizations. The inverse consistency loss becomes helpful to better reconstruct shapes when using zero-padding strategy.

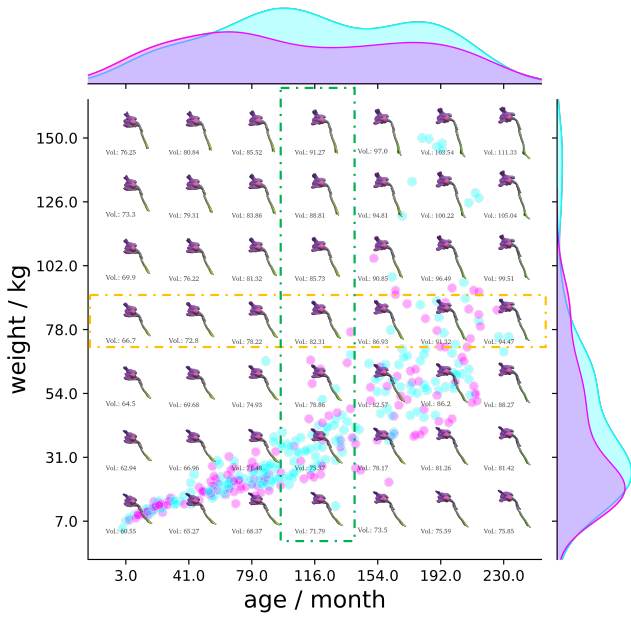


Figure 6. Shape extrapolation in covariate space (for a different patient in the testing set than the one in the main text). Example shapes in the age-weight space are visualized with their volumes (cm^3) below. Cyan points represent male and purple points female children in the dataset. The points represent the covariates of all children in the dataset. The colored shades represent the age and weight distributions stratified by sex. The latent code \mathbf{z} is kept constant to create an individualized covariate shape space. The shapes in the green and yellow boxes are plotted with $\{\Phi_i\}$ (see Sec. 3.4), representing the disentangled shape evolutions along weight and age respectively. Shapes extrapolated from \mathbf{z}_i look realistic and smooth across different covariates. (Best viewed zoomed.)

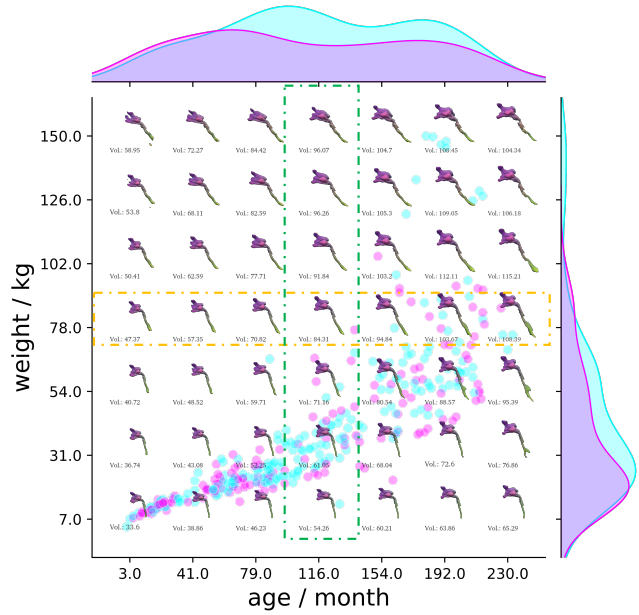


Figure 7. Shape extrapolation in covariate space for an average airway shape from $\bar{\mathbf{z}}$ (from Eq. (19)). Example shapes in the age-weight space are visualized with their volumes (cm^3) below. Cyan points represent male and purple points female children in the dataset. The points represent the covariates of all children in the dataset. The colored shades represent the age and weight distributions stratified by sex. The latent code \mathbf{z} is kept constant to create an individualized covariate shape space. The shapes in the green and yellow boxes are plotted with $\{\Phi_i\}$ (see Sec. 3.4), representing the disentangled shape evolutions along weight and age respectively. The extrapolated shape space from $\bar{\mathbf{z}}$ is able to reflect the overall shape development tendency in the large population; it corresponds better with the population shape development shown in Tab. 6. (Best viewed zoomed.)

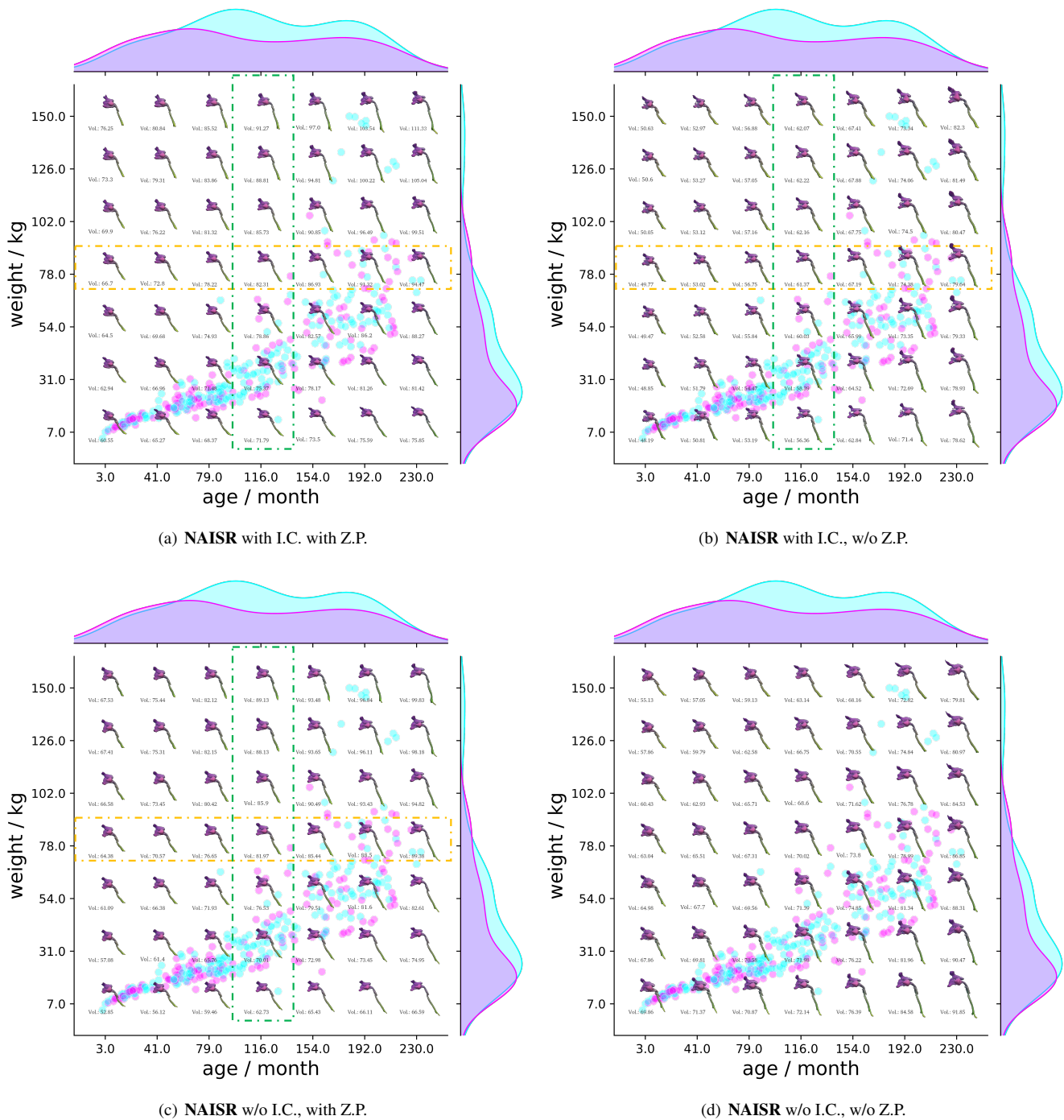
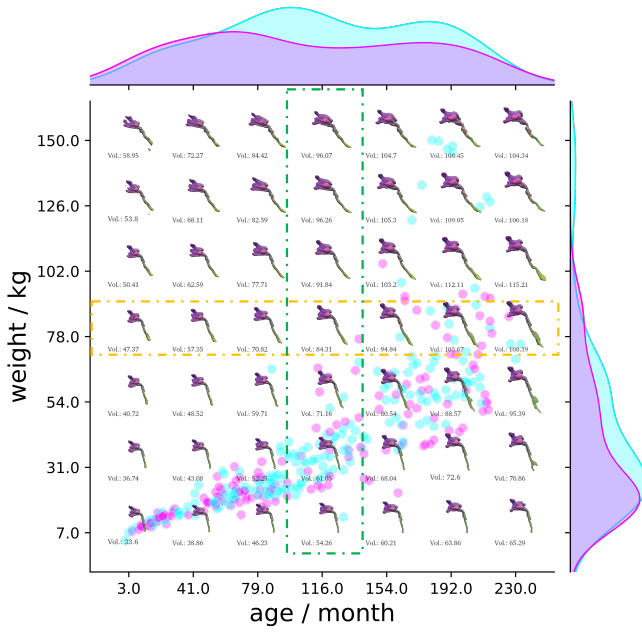
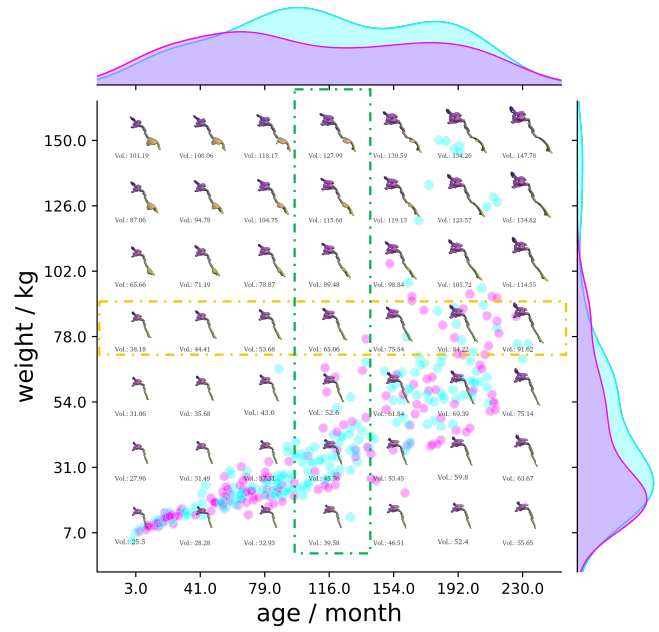


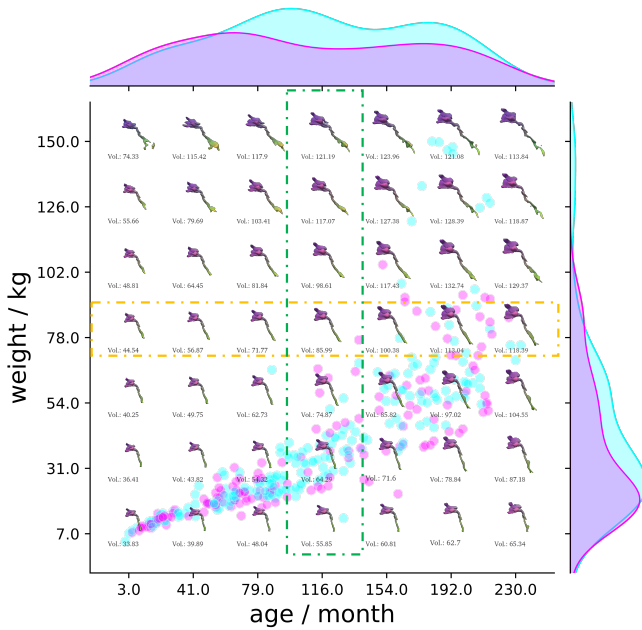
Figure 8. Comparisons of shape extrapolation for different experiment settings from \mathbf{z}_i for one patient. I.C. denotes that the inverse consistency loss was used. Z.P. denotes that the zero-padding strategy was used to encourage interpretability. Example shapes in the age-weight space are visualized with their volumes (cm^3) below. Cyan points represent male and purple points female children in the dataset. The points represent the covariates of all children in the dataset. The colored shades represent the age and weight distributions stratified by sex. The latent code \mathbf{z} is kept constant to create an individualized covariate shape space. The shapes in the green and yellow boxes are plotted with $\{\Phi_i\}$ (see Sec. 3.4), representing the disentangled shape evolutions along weight and age respectively. NAISR is able to produce realistic shapes with all experiment settings. However, the network has difficulty evolving shapes along weight when the zero-padding strategy is not used.



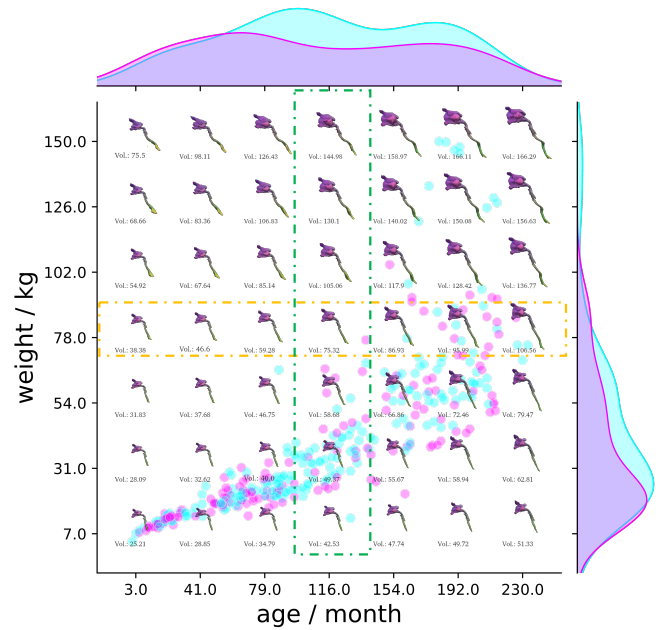
(a) NAISR with I.C. with Z.P.



(b) NAISR with I.C., w/o Z.P.



(c) NAISR w/o I.C., with Z.P.



(d) NAISR w/o I.C., w/o Z.P.

Figure 9. Comparisons of shape extrapolation for different experiment settings from \bar{z} for an average airway shape. I.C. denotes that the inverse consistency loss was used. Z.P. denotes that the zero-padding strategy was used to encourage interpretability. Example shapes in the age-weight space are visualized with their volumes (cm^3) below. Cyan points represent male and purple points female children in the dataset. The points represent the covariates of all children in the dataset. The colored shades represent the age and weight distributions stratified by sex. The latent code \mathbf{z} is kept constant to create an individualized covariate shape space. The shapes in the green and yellow boxes are plotted with $\{\Phi_i\}$ (see Sec. 3.4), representing the disentangled shape evolutions along weight and age respectively. All settings can evolve the airway shapes reasonably if there are enough data points in the covariate space, indicating that NAISR is able to capture the airway development tendency of the population. However, all settings may produce unrealistic airways for unseen covariates. (Best viewed zoomed.)